GDCh Research Article Angewandte International Edition Chemie www.angewandte.org

How to cite: *Angew. Chem. Int. Ed.* **2025**, *64*, e202505523
doi.org/10.1002/anie.202505523

Inorganic Nanoparticles

A Programmable Nanoparticle Conversion Pathway to Monodisperse Polyelemental High Entropy Alloy, Intermetallic, and Multiphase Nanoparticles

*Nabojit Kar, Alberto Leonardi, Maximilian McCoy, Rukshanthan Selvaraj, and Sara E. Skrabalak**

Abstract: Polyelemental nanoparticles (PE NPs), those consisting of four or more elements, exhibit unique properties from synergistic compositional effects. Examples include high entropy alloys, high entropy intermetallics, and multiphase types, including Janus and core-shell architectures. Although colloidal syntheses offer excellent structural control for mono- and bi-elemental compositions, achieving the same control for PE NPs remains challenging. Here, this challenge is addressed with a NP conversion strategy wherein different types of PE NPs – including high entropy alloy, high entropy intermetallic, and multiphase Janus nanoparticles – are achieved through thermal transformation of readily synthesized colloidal core-shell NPs. Through systematic variations in stoichiometry and metal identity to the core-shell precursor NPs, along with atomistic simulations that probe phase stabilities, we deduce that the final mixing states of the various NPs are governed by the balance between the enthalpy and entropy of mixing. Moreover, our annealing method allows us to trap NPs at intermediate states of mixing, creating distinct surface ensembles that were evaluated as catalysts for the hydrogen evolution reaction. This study is the first, to our knowledge, to report colloidally derived precursor NPs enabling the synthesis of all types of PE NPs in a single process. This NP conversion strategy offers a general route to diverse PE NPs.

Introduction

Polyelemental nanoparticles (PE NPs), those consisting of four or more elements, often exhibit synergistic physical and chemical properties compared to their single-element counterparts.[1–4] Crystalline PE NPs are categorized by their phases (e.g., alloys or intermetallics) and the structural arrangement of the phases when more than one is present (e.g., Janus, core-shell, or triphasic). For example, high entropy alloys (HEAs) are single-phase solid solutions that form on account of their high configurational entropy.[5–8] Quantitatively, PE systems evolve toward minimizing ΔG_{mix} in Equation (1),

$$\Delta G_{mix} = \Delta H_{mix} - T\Delta S_{mix} \quad (1)$$

where ΔG_{mix} is the Gibbs free energy of mixing, ΔH_{mix} is the enthalpy of mixing, ΔS_{mix} is the entropy of mixing, and T is temperature. Thus, HEAs form when the $T\Delta S_{mix}$ term drives the system.[9] High entropy intermetallics (HEIs) are related to HEAs but exhibit extended-range chemical ordering through the emergence of sublattices, but with random mixing within at least one sublattice.[10,11] The crystal structures of HEI NPs resemble that of their binary intermetallic counterparts, where metals with similar properties (e.g., atomic radius and electronegativity) occupy distinct sublattices, leading to a negative $\Delta H_{mix.}$[12–16] In contrast, multiphase systems arise when $T\Delta S_{mix}$ cannot offset a positive ΔH_{mix} for certain alloy compositions, creating unique interfaces that define the electronic interactions between phases.[17–19] Although these NPs exhibit significant potential, their synthesis remains nontrivial, but emerging techniques such as lithographically defined nanoreactors[17] and carbothermal shock[20,21] offer some control.

Colloidal methods stand out for their accessibility and structural control in simpler compositions, which typically involve heating metal precursors with capping agents present. With judicious selection of reaction conditions, monodisperse HEA and HEI NPs have even been achieved.[22–27] Mechanistic studies highlight that these NP formation occurs through complex processes.[8,28,29] For example, Soliman and

[*] N. Kar, M. McCoy, R. Selvaraj, S. E. Skrabalak
Department of Chemistry, Indiana University, Bloomington, IN 47405, USA
E-mail: sskrabal@indiana.edu
sskrabal@iu.edu

A. Leonardi
Physical Sciences, Diamond Light Source (United Kingdom), Diamond House – Harwell Science & Innovation Campus, Didcot, Oxfordshire OX11 0DE, UK

A. Leonardi
Earth and Atmospheric Sciences, Indiana University, 1001 East 10th street, Bloomington, Indiana 47405-1405, USA

Additional supporting information can be found online in the Supporting Information section

coworkers studied the formation of HEI (Pd, Rh, Ir, Pt)Sn NPs in a heated solution of oleylamine and octadecene.[29] By performing a time-point study, they found Pd-enriched Pd-Sn NPs formed first, with the other metals depositing onto the seeds over time, concomitant with the incorporation of additional Sn interdiffusion, resulting in NPs with both flower-like and cube-like morphologies. These observations are unsurprising, given the distinct reactivity profiles of each metal precursor.[24] These observations also suggests that new colloidal syntheses will have to be developed for even small variations in PE NPs, much like how the area of bimetallic NP synthesis has developed.[30,31] Yet, this mechanistic study also sheds light on an alternative pathway to PE NPs, where the observation of bimetallic NPs in the early stages of the synthesis followed by additional metal deposition and metal mixing, suggests that such single-step NP syntheses can be broken into a multistep seeded process, where compositionally simple NPs can serve as seeds to build up core-shell NPs consisting of the requisite metals that are then thermally converted into the desired PE NP type.

This thought experiment highlights the value of NP conversion pathways, where simpler precursor NPs are transformed into target NPs via chemical or physical methods. In fact, we showed that PE core-shell NPs with five elements can be annealed into HEA NPs.[32,33] In contrast to direct colloidal synthesis of HEAs, this approach requires fewer metal precursors at each step, enabling the formation of monodisperse HEA samples with significantly greater synthetic control.[34] However, this NP conversion method has not been shown to synthesize every type of PE NP and the general applicability of the process, grounded in thermodynamic principles, has not been presented previously. In this work, we demonstrate the generality of this NP conversion strategy to synthesize HEA, HEI, and multiphase NPs by considering the stoichiometry and metal identities in the precursor PE core-shell NPs. Results show that annealing nonequimolar core-shell Au_xCu_{1-x}@PtPdM (M = Ni or Fe) NPs leads to the formation of AuCuPd-PtM (M = Ni, Fe) Janus NPs. Additionally, we found that equimolar core-shell NPs promote homogeneous mixing rather than phase segregation, synthesizing AuCuPtPdNi and AuCuPtPdFe NPs, where Fe incorporation favors HEI phase formation and Ni incorporation enhances HEA phase formation. The central hypothesis is that the formation of these materials is governed by the interplay between enthalpy and entropy of mixing, which collectively influences the Gibbs free energy of mixing. To the best of our knowledge, this is the first report of colloidally derived precursor NPs providing access to all types of PE NPs in a single process. These insights provide a programmable synthetic pathway to a library of PE NPs.

Results and Discussion

Evaluation of PE Core-Shell NP Stoichiometry and the Synthesis of Multiphase Janus Nanoparticles

Recall that ΔS_{mix} competes with ΔH_{mix} to determine whether a HEA phase is favorable. This relationship suggests that ΔS_{mix} would be maximized with PE core-shell NPs of equimolar constituent metals and that multiphase PE NPs may be favored when ΔS_{mix} is lowered by selecting nonequimolar precursor PE core-shell NPs. Previously, we reported the synthesis of equimolar core-shell NPs and their thermal conversion to HEA NPs.[33,34] Thus, we hypothesized that precursor PE core-shell NPs with nonequimolar stoichiometries could be prepared and serve as precursors to multiphase PE NPs (Figure 1). Specifically, Au_2Cu and $AuCu_2$ seeds (Figures S1, S2) were prepared by standard methods,[35] followed by core-shell NP syntheses where PtPdNi shells were deposited by coreduction of $PtBr_2$, $PdBr_2$, and $Ni(acac)_2$ in a heated solution. The resulting core-shell Au_2Cu@PdPtNi and $AuCu_2$@PdPtNi NPs ("@" denotes the core-shell interface) are shown in Figures S3, S4. These precursor NPs were then dispersed on a carbon support and annealed under forming gas at 800 °C for 2 h. Figure 2a–d shows the characterization of the multiphase Janus Au_{rich}CuPd-PtNi NPs, which were annealed from the core-shell Au_2Cu@PdPtNi precursor NPs. Here, the "-" denotes the interface of the two domains comprising the Janus NPs. Transmission electron microscopy (TEM) of Au_{rich}CuPd-PtNi NPs, converted from 10.1 ± 1.2 nm core-shell Au_2Cu@PdPtNi NPs, shows an average size (diameter) of 9.2 ± 1.0 nm, indicating preserved monodispersity (10% standard deviation) (Figures 2a and S5). Note that NP shape changes during annealing, and measurements on the carbon support may account for the slight size deviations. Scanning transmission electron microscopy coupled with energy dispersive X-ray spectroscopy (STEM-EDS) (Figures 2b and S6) and line scan analysis (Figure 2c) show that Au, Cu, and Pd are located on one side of the NPs, whereas Pt and Ni are located on the other side, supporting formation of Janus NPs. The elemental distribution is distinct from the precursor core-shell NPs (Figure S3b,c,f,g). X-ray diffraction (XRD) shows two sets of fcc reflections, which match calculated AuCuPd and PtNi alloy references from Vegard's law based on the elemental data from inductively coupled plasma mass spectrometry (ICP-MS) and EDS (Figure 2d). The broad reflection around 45° 2θ is from the carbon support (Figure S7). High-resolution (HR) TEM shows the lattice fringes of two domains of the Janus NP are 1.974 and 1.8 Å, which correspond to the (200) planes of the AuCuPd and PtNi alloy phases, respectively (Figure S8). The atomic percentages (at. %) of elements in the Janus NPs and core-shell NPs obtained via ICP-MS match well with each other and are also consistent with the at. % of the core-shell Au_2Cu@PdPtNi NPs obtained from elemental analysis using scanning electron microscopy (SEM)-EDS and STEM-EDS (Figures S9 and S3i), indicating negligible metal evaporation during annealing. X-ray photoelectron spectroscopy (XPS) shows atomic percentages of Au (36 at. %), Cu (16 at. %), Pt (12 at. %), Ni (12 at. %), and Pd (26 at. %) (Figure S10), which matches well with the ICP-MS and EDS analysis while accounting for the surface sensitivity of the technique.

Annealing the core-shell $AuCu_2$@PdPtNi NPs (size 12.7 ± 1.3 nm, Figure S4a) also leads to the formation of Janus NPs, in this case $AuCu_{rich}$Pd-PtNi NPs with an average size (diameter) of 11.2 ± 1.8 nm (Figures 2e and S11). Figure 2e–f shows the characterization of the multiphase

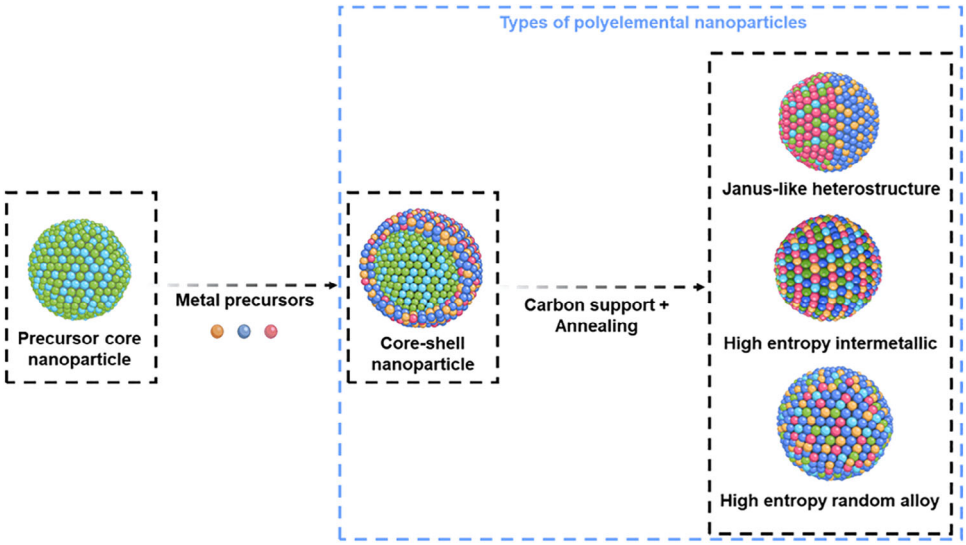

Figure 1. Illustration of the nanoparticle (NP) conversion process to synthesize different polyelemental (PE) NPs. The process starts with bimetallic seeds, then, three shell metals are added as trimetallic alloy shells, creating core-shell NPs. These core-shell NPs, consisting of five metals are then dispersed on a carbon support and annealed to facilitate intermixing and the formation of PE NPs.

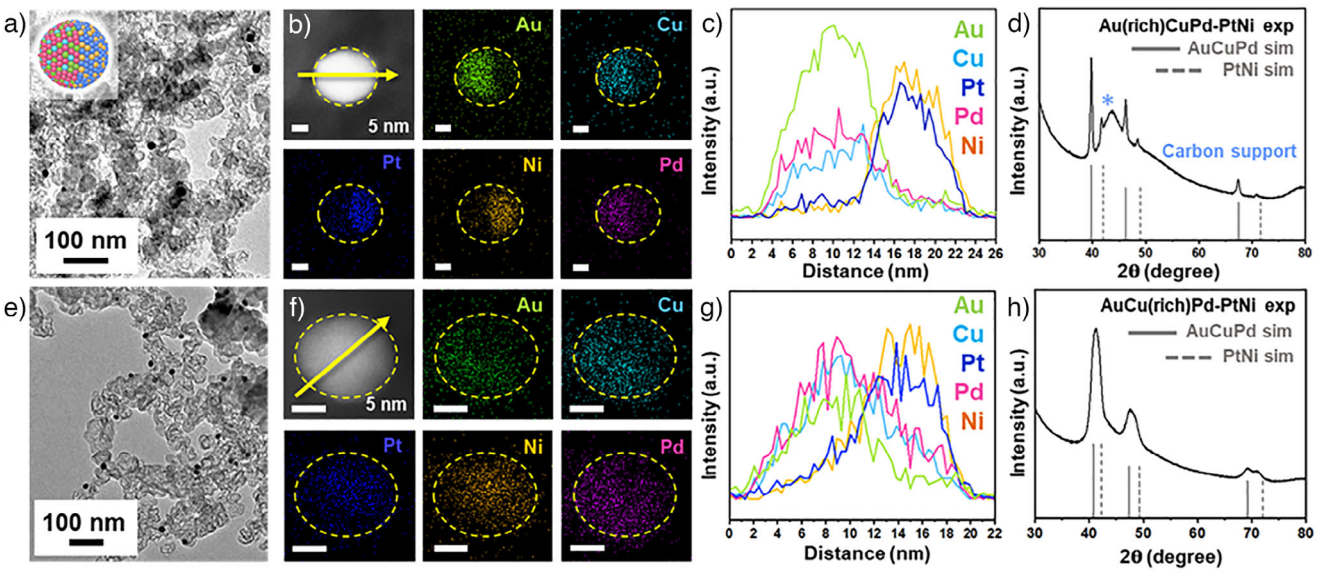

Figure 2. Morphological and elemental characterization of monodisperse multiphase AuCuPd-PtNi NPs. Transmission electron microscopy (TEM) images with NP model in inset a), e), Scanning transmission electron microscopy coupled with energy dispersive X-ray spectroscopy (STEM–EDS) elemental mapping b), f), linescan analyses according to yellow lines c), g), and X-ray diffraction (XRD) patterns d), h) of the samples AurichCuPd-PtNi a)–d) and AuCurichPd-PtNi NPs. d), h) Alloy references for XRD were calculated by applying the experimental elemental composition by atomic percentage (at %) to Vegard's law.

Janus $AuCu_{rich}$Pd-PtNi NPs. ICP-MS, SEM-EDS, and STEM-EDS of the core-shell NPs show high Cu in the system (Figure S4i). The STEM-EDS map and line scan of the annealed NPs show PtNi phase segregation from the rest of the elements Au, Cu, and Pd (Figure 2f–g). The XRD pattern does not have a distinct peak difference like the previous Janus NPs, which is consistent with the similar lattice parameters for the two anticipated phases. However, the XRD reflections are broadened and split into two distinct reflections at high 2θ (around 70° 2θ), confirming the two phases (Figure 2h).

We also examined the generality of precursor PE core-shell NPs with nonequimolar stoichiometries to produce multiphase NPs upon annealing by preparing core-shell Au_2Cu@PtPdFe and $AuCu_2$@PtPdFe NPs by a similar method (Figures S12 and S13). These NPs were dispersed on carbon and annealed, where Pt and Fe phase-segregate together and Au and Cu phase-segregate together, with Pd found throughout the NP but with an inclination to alloy with Au and Cu (Figure S14). Interestingly, the XRD patterns show reflections at low 2θ indicative of intermetallic phases (Figure S14d,h);

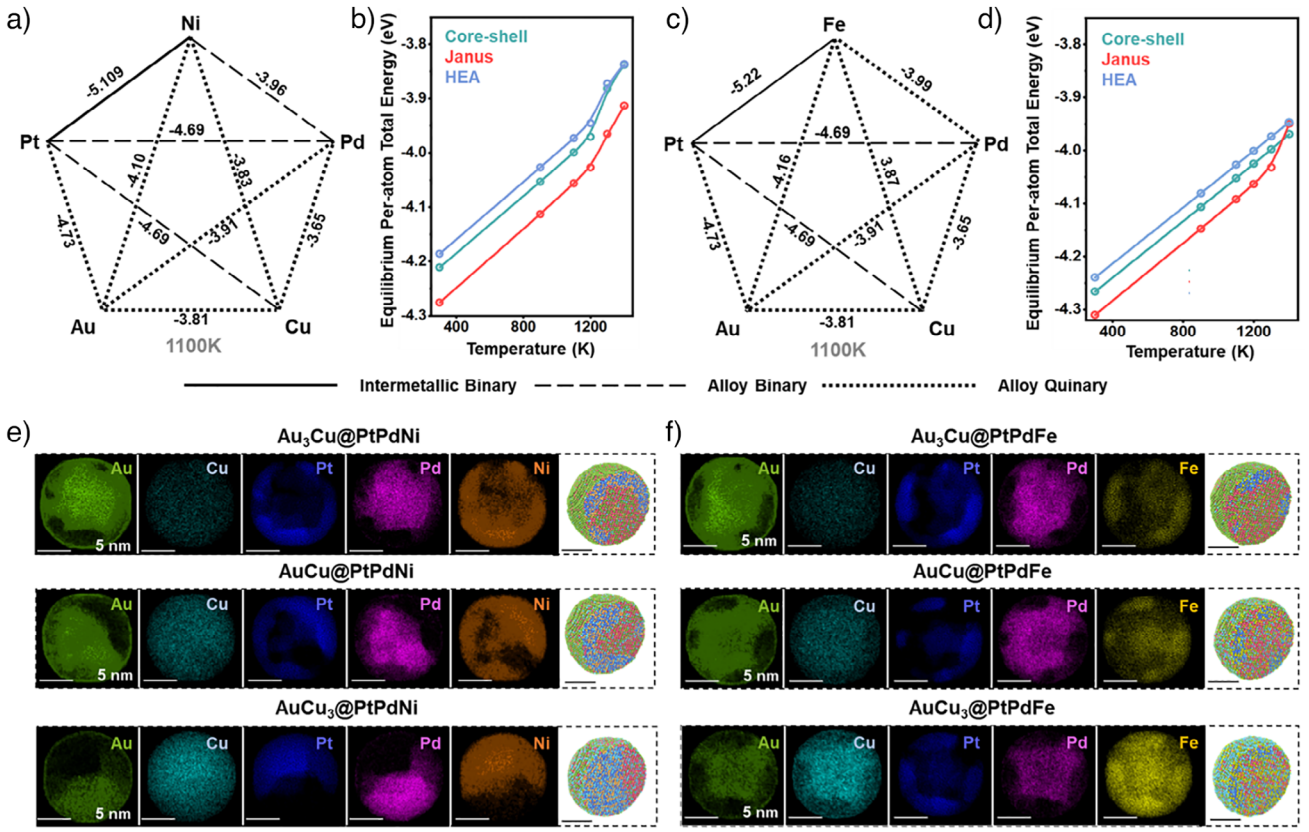

Figure 3. Atomistic simulations of the Au_xCu_{1-x}@PtPdM (M = Ni or Fe) NPs a) and c), Equilibrium bond-like energy (eV) of atom pair for most stable phase or most stable bond configuration for a). Au-Cu-Pt-Pd-Ni and c). Au-Cu-Pt-Pd-Fe systems. Here, binary intermetallic, binary alloy, and quinary alloy is denoted by continuous line, dashed line, and dot line respectively. b) and d), Temperature versus average per-atom potential energy graphs showing the stability of phases when annealed (note: the lower the energy, the more stable the configuration), respectively for $Au_3CuPdPtNi$ and $AuCu_3PdPtFe$ NPs. e) and f), STEM-EDS simulations from 100 zone axis for core@shell configurations with cross-sectional model for Au_xCu_{1-x} core with e). PtPdNi and f. PtPdFe in the shell for $x = 0.75$, 0.50, and 0.25 after annealing at 1100 K or ~800 °C. All scale bars are 5 nm.

however, the alloy phases are not distinguishable from one another due to overlapping reflections.

The multiphase NPs were anticipated from precursor PE core-shell NPs with nonequimolar stoichiometries, but predicting specific phases a priori is difficult due to the many bonding interactions that define the enthalpy and entropy of the system. By examining the bond dissociation energies for all possible metal pair combinations, we can predict that metals with stronger bonds will tend to segregate together, while those with weaker bonds are more likely to alloy.[36] Figures 3 and S15–S26 show the atomistic simulations where we varied starting core-shell stoichiometry (ideal equimolar - AuCu@PtPdM - to nonequimolar cores - Au_3Cu@PtPdM and $AuCu_3$@PtPdM, where M is Ni or Fe), core-shell NP size (8–14 nm), and match stoichiometries from experiments considering colloidal synthesis limitations (Table S1). Although the bonding energies of metallic species are affected by the embedding energy of the particles' body electron density,[37] we compared the per-bond enthalpy energy of the different elemental pairs from given equimolar cubic structures, i.e., binary intermetallic, binary random alloy, and quinary random alloy (Figures 3a,c, S15, and S16). Equilibrium molecular dynamics (MD) simulations confirm that Pt-Fe and Pt-Ni bonds are the strongest regardless of the structural configuration and temperature (Figure 3a,c). These pairs are also the only with the strongest per-bond enthalpy observed for the intermetallic phase. Bonds between Au, Cu, Pd, and Fe or Ni, except Pd-Ni, show a preference for random quinary alloy mixing with the lowest per-bond enthalpy, whereas the per-bond Pt enthalpies with nonAu elements favor binary mixing (Figure 3a,c). Thus, the differentiating factor governing the structural configuration is the strong bond between Pt and either Ni or Fe, where their segregation results in optimizing all the bond energy pairs in the Janus NPs. Hybrid Monte Carlo (MC)-MD simulations of PE NPs show evidence of the per-bond enthalpy energy affecting the kinetics of transformation during annealing at various temperatures (300–1400 K) (Supporting Video 1–3), followed by being quenched to room temperature (Supporting Video 4–6). We simulated STEM-EDS maps of the PE NPs from the atomistic simulations for comparison to experiment (Figures S17, S18, and S24–S26). The Ni-based NPs show a stronger tendency toward Janus-like configurations compared to the Fe-based NPs (Figure 3e,f).[36]

Notably, Pt favors quinary alloy mixing only with Au, making the relative amount of Cu a key driver for the elemental segregation during the annealing of these systems. Lower than only the Pt-Ni and Pt-Fe pairs, we observed the

largest per-bond enthalpy gap of binary versus quinary configurations for Cu-Pt ($\geq$ 0.3 eV against $\leq$ 0.13 eV) (Figures S15 and S16). Here, Pt-X range between 0.30 and 0.43 eV, Cu-Pt range between 0.16 and 0.25 eV, and others range between −0.32 and 0.13 eV, with a positive gap favoring binary against quinary. These energy gaps account for the tendency toward Janus-like segregation observed in the hybrid MC-MD kinetic transformation of $AuCu_3$@PtPdNi NPs compared to the Au_3Cu@PtPdNi and AuCu@PtPdNi NPs. For the Fe-system we don't observe clear Janus NP formation. Although the energy gaps and bond-type stability are consistent with the Ni-system, the substitution of Fe for Ni affects the per-atom equilibrium energy in the quinary random alloy mix. We compute the stability for the bonds in the quinary alloy configuration to increase between 0.02 to 0.06 eV, which is between 14% and 41% of the average per-bond enthalpy gap of binary versus quinary configurations.

Simulations suggest a structure's anisotropy (i.e., lower packing fraction along the <h00> direction compared to <hhh>) is another key driver to elemental segregation (Figure S19).[38,39] Directional preferential segregation is observed in the STEM-EDS simulations for the Au_3Cu core-based and Fe-based NPs (Figure 3e,f). The tendency for elemental segregation is also enhanced for smaller crystal sizes. Janus-like NPs start appearing at 900 K (626.85 °C) for 8 nm sized NPs compared to 1300 K (1026.85 °C) for 16 nm (Figures S20–S23). We attribute this behavior to the larger surface relaxation and enhanced mechanical anisotropy properties of small sized NPs. The elemental segregation observed for Fe-based NPs can then be explained by the different equilibrium structure of Fe compared to the other pure elements (i.e., bcc against fcc). Furthermore, the embedding environments in real experiments can then explain significant differences in transformation kinetics observed compared with our idealized simulations in a vacuum.

Synthesis of High Entropy Intermetallic and High Entropy Random Alloy Nanoparticles

Intermetallic phases (Figure S14h) in the multiphase NPs from precursor PE core-shell NPs with nonequimolar stoichiometries suggests that Fe addition promotes a negative ΔH_{mix}, which could potentially be leveraged to achieve HEI NPs when the precursor PE core-shell NPs are equimolar, and multiphase NPs are less favored. However, in our previous study, annealing PdCu@PtNiFe NPs produced HEA PdCuPtNiFe NPs despite Pt and Fe in the system (Figure S27). Recently, Au has been shown to promote mixing and lower the disorder-to-order phase transition temperature ($T_{PT\,d\rightarrow o}$) in PtFe, thus enabling intermetallic formation at lower temperatures.[40,41] Based on these observations, we hypothesized that equimolar NPs with AuCu cores and Pt, Fe, and Pd shells could result in HEI NPs upon annealing.

First, equimolar AuCu alloy NPs (size 8.2 ± 0.9 nm) were synthesized (Figure S28).[42] Then, these NPs were used as seeds to synthesize core-shell AuCu@PtPdFe NPs, where PtPdFe shells were deposited by coreduction of $PtBr_2$, $PdBr_2$, and $Fe(acac)_3$ in heated solution (Figure S29). These precursor core-shell NPs were dispersed on carbon and annealed at 800 °C under forming gas for 2 h. Figure 4a–h presents the characterization of the annealed product: HEI AuCuPtPdFe NPs. The annealed HEI NPs are monodispersed by TEM (~10.3 ± 0.9 nm) (Figure 4a). STEM-EDS and line scans show the metals are homogenously mixed at the nanoscale (Figure 4b,c). XRD matches both the intermetallic $L1_0$ fct-PtFe and $L1_2$-Pt_3Fe structures, which have similar lattice parameters (Figure 4d). High-magnification STEM of a HEI AuCuPtPdFe NP shows alternating dark and bright atom layers, and the d-spacing between the lines matches well with the (200) planes of the PtFe intermetallic phase (Figure 4e). The high-resolution EDS elemental mapping and line profile show distinct lattices formed by Pt and Fe signals (Figure 4f,g). Pd signals are associated with the Pt lattice. Based on Z-contrast, atomic size, and electronegativity, we propose that Au and Pd associate within the Pt sublattice, while Cu is associated with the Fe sublattice. Given the composition of the precursor core-shell NPs (Au 19.5 at. %, Cu 15 at. %, Pt 20 at. %, Pd 23 at. %, and Fe 23 at. %), this finding suggests there may be a mixture of HEI phases, with different sublattice occupancies. XPS shows atomic percentages of Au (25 at. %), Cu (16 at. %), Pt (16 at. %), Fe (22 at. %), and Pd (21 at. %) (Figure S31). The XPS data show all metals are within the at. % range of 16%–25%, which is consistent with the starting equimolar core-shell NPs.

Binary alloy phase diagrams indicate that intermetallic compounds form more readily below the $T_{PT\,d\rightarrow o}$ and an annealing temperature near or above $T_{PT\,d\rightarrow o}$ hinders the disorder-to-order transition.[43] Therefore, an annealing temperature of ~800 °C for the equimolar precursor core-shell NP favors the formation of disordered or random alloy to ordered intermetallic either $L1_0$ fct-PtFe or $L1_2$-Pt_3Fe phases (Pt-Fe system $T_{PT\,d\rightarrow o}$ ~1300 °C) but theoretically should be unfavorable for intermetallic $L1_0$ fct or $L1_2$ Pt_xNi_{1-x} phases (Pt-Ni system $T_{PT\,d\rightarrow o}$ ~630 °C) (Figure S32). To evaluate this concept, we synthesized equimolar core-shell AuCu@PdPtNi NPs using the same AuCu NPs as seeds (Figure S33). The resulting NPs were then annealed at 800 °C under forming gas for 2 h. Figure 4i–l presents the characterization of the annealed product NPs. The product is monodispersed by TEM (10.7 ± 0.7 nm and 10.0 ± 0.9 nm for AuCu@PdPtNi and AuCuPdPtNi NPs, respectively (Figure S34). A significant population of AuCuPdPtNi NPs with a fcc phase formed (53%), which is consistent with equimolar precursor core-shell NPs yielding single-phase systems. The sample also includes intermediate mixed particles and Janus-like particles, with populations of 26% and 21%, respectively (Figures S35 and S36). The XRD pattern shows different phases, consistent with the mixture of HEA and heterostructure NP products (Figure 4l). STEM-EDS and line scan of HEA products show all metals are mixed homogenously at the nanoscale (Figure 4j,k). High-resolution STEM shows similar z contrast in each plane, and the EDS elemental map does not show any segregation (Figure S37). The layer spacing matches well the (111) and (200) d-spacing values from XRD.

According to theoretical calculations, when all five metals are equimolar, the configurational entropy of the system is maximized (Table S2). The annealing of equimolar

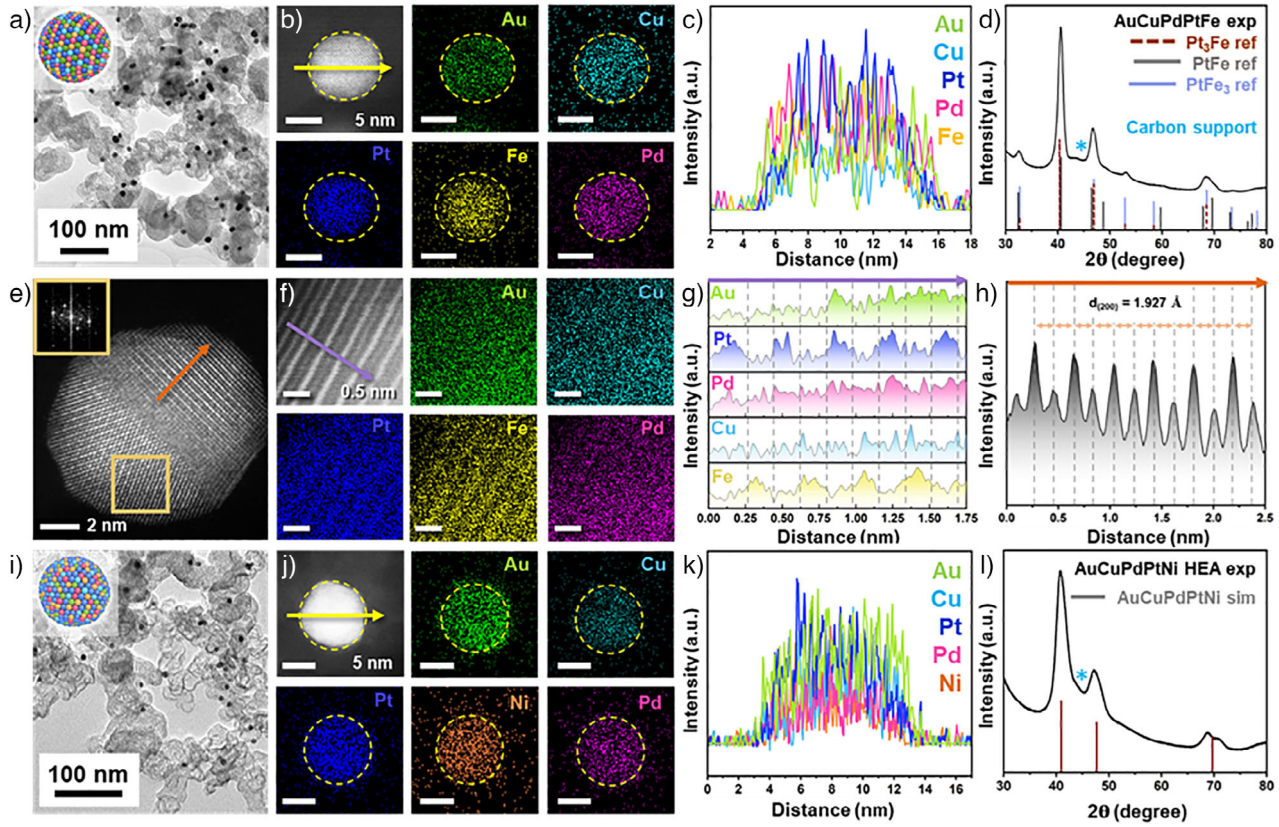

Figure 4. Morphological and elemental characterization of monodisperse high-entropy intermetallic and high-entropy alloy NPs. a)–l), TEM images with NP model in inset a) and i), STEM–EDS elemental mapping b) and j), linescan analysis according to yellow lines c) and k), X-ray diffraction (XRD) pattern d) and l) of the AuCuPtPdFe a)–d) and AuCuPtPdNi i)–l). e) High-angle annular dark-field scanning transmission electron microscopy (HAADF)-STEM and f) high magnification STEM-EDS elemental mapping of an HEI AuCuPtPdFe NP with FFT area of corresponding yellow box in inset. Linescan analysis from the (g) HAADF-STEM in (f) as denoted by the purple line and extracted from the yellow box in (e) as well as (h) from the HAADF-STEM in (e) as denoted by the orange line. XRD of alloy references were calculated by considering the elemental composition by at% and Vegard's law.

AuCu@PdPtFe NPs leads to single-phase HEI NPs. We also observed that annealing equimolar AuCu@PdPtNi NPs predominantly results in the formation of HEA NPs (53%). These observations underpin the effect of ΔH_{mix} in the final product depending on the composition of the precursor NPs. MC-MD simulations show the enthalpy of the phase-segregated product (Janus) is lowest (i.e., most favorable), although all configurations approach the same value with increasing temperature (Figures 3b,d, and S38). Consistent with experimental observations, the MC-MD transformation paths indicate that, despite enthalpy differences, alloy mixed or partially segregated phases are more likely to form at lower annealing temperatures (<977 K). This observation confirms that entropy is the driving force for the phase transformations. With the temperature approaching the melting point, the dynamic component of entropy (S_{vib}) dominates over the configurational component (S_{config}). Given S_{vib} only depends on temperature for equi-composition NPs, the enthalpy gradients of different configurations drive the annealing products, enthalpy minimum, i.e., the phase-segregated products. At low annealing temperatures, while entropy promotes overall elemental mixing, the stronger per-bond enthalpy of Pt-Fe compared to Pt-Ni, combined with the preference for Pd-Fe in quinary alloys over Pd-Ni in binary alloys, explains why HEI phases are favored over HEA phases for AuCu@PtPdFe and AuCu@PtPdNi, respectively. We note that, although intraparticle heterogeneity—previously discussed in our earlier work—is challenging to detect experimentally, both our current experimental data and simulations provide no evidence for its presence in this study.[33] Surface relaxation-induced segregation likely prevents our simulations from unequivocally supporting the formation of HEI or HEA NPs from equimolar core-shell PE NPs. The phase segregation observed in MC-MD simulations does not conform to the Janus configuration but rather to the mechanical anisotropy of the cubic structure. Similarly, as grain boundaries are known to drive segregation in HEAs, the lack of a bounding C-matrix at the surface of the NP in our simulations alters the energy of atoms at the surface and, consequently across the NP body.

Engineering the Surface Ensemble Sites of PE NP Catalysts

The performance of NP catalysts is closely linked to the adsorption strength and configuration of reactive molecules at the NP surface, influenced by ligand effects, geometric

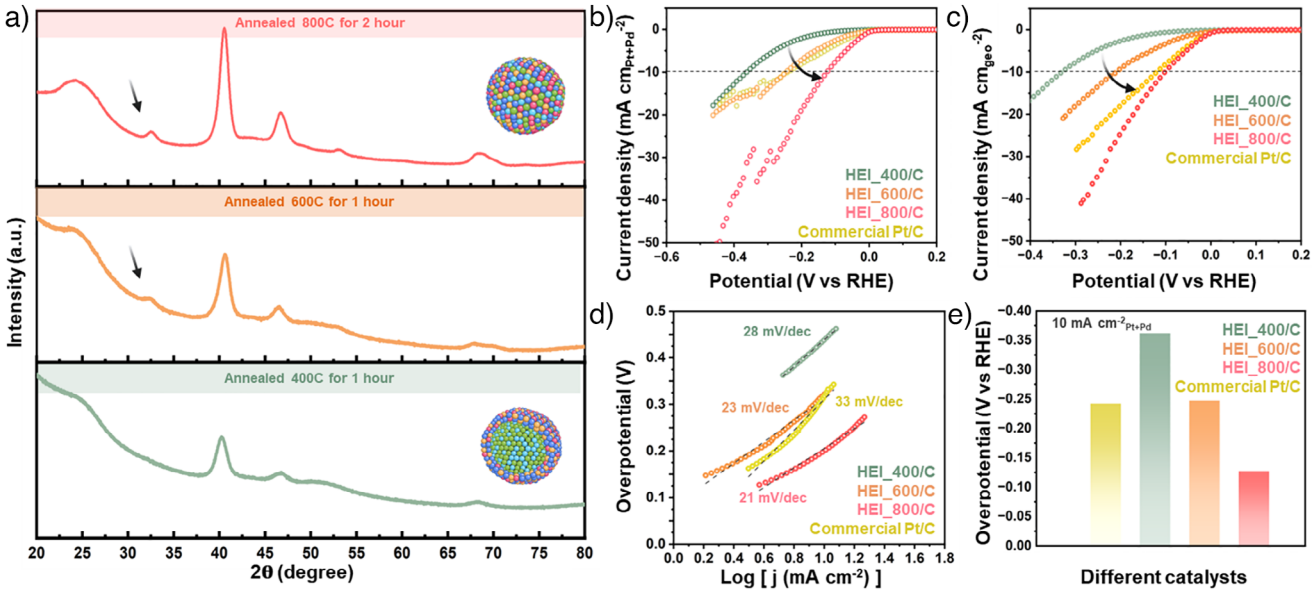

Figure 5. Electrochemical performance of AuCuPtPdFe HEI NPs toward HER in an N2-purged 1 M KOH solution. a) XRD patterns of AuCuPtPdFe catalysts with different ordering degrees with the NP models. Black arrow shows the generation of intermetallic phase reflection. b) HER LSV curves of 20% commercial Pt/C, HEI_400/C, HEI_600/C, and HEI_800/C, normalized by loading mass of Pt and Pd. c) HER LSV curves normalized by geometric area. d) The corresponding Tafel plots were calculated from the HER polarization curves normalized by loading mass of Pt and Pd. e) Comparison of overpotentials at 10 mA cm^{-2} between AuCuPtPdFe catalysts with different ordering degrees and commercial Pt/C.

strain, and ensemble effects.[44,45] Ensemble effects arise from variations in surface atom groupings (small ensembles of surface atoms), leading to changes in the adsorption configuration, energy, and repulsion of reactive molecules at active sites. Given that the final NP evolution closely aligns with thermodynamic predictions, we hypothesized that annealing would shift the equilibrium—particularly the entropic contribution—as the system temperature varies. To explore this, we annealed the core–shell nanoparticles at two distinct temperatures (600 and 800 °C) to probe the temperature-dependent balance between enthalpic and entropic factors and assessed/correlated the resulting surface ensemble configurations with their electrocatalytic performance. We specifically evaluated the HER performance of core-shell AuCu@PtPdFe NPs and compared these results to partially ordered and fully ordered HEI NPs, achieved by annealing the carbon supported core-shell NPs at different temperatures and times (denoted as HEI_600/C and HEI_800/C for annealing at 600 °C for 1 h and 800 °C for 2 h, respectively). To remove capping agents, the core-shell NPs were also dispersed on carbon and annealed at 400 °C, designated as HEI_400/C. XRD patterns indicate the formation of intermetallic phases in the HEI_600/C and HEI_800/C samples, as evidenced by the intense superlattice peak around 32° 2θ (with the sample annealed to higher temperature having a higher intensity intermetallic reflection, suggesting more HEI phase formation). In contrast, no intermetallic phase is observed for the HEI_400/C sample (Figure 5a). STEM-EDS elemental mapping of the HEI_400/C NPs shows core-shell architectures, but the HEI_600/C NPs show an intermediate stage of mixing (Figure S39). In all of the cases, the loading of catalysts was kept at 10 wt% by ICP-MS. A standard three-electrode system with 1 M KOH aqueous solution was used, as conventional methods—especially in acidic media—are often unable to quantify HER kinetic rates due to the exceptionally fast kinetics of HER on Pt surfaces.[46] The HER was selected due to its technological significance[47] and the need for stable HER catalysts composed of earth-abundant elements, especially in basic media, which is commonly employed in industrial water splitting.[48–50]

Figure 5b–e show HER electrochemical performance data for the various surface engineered NP samples. The potential required to reach a current density of 10 mA cm^{-2} is a key indicator to evaluate the HER performance. Each experiment was carried out three times and averaged. As shown by linear sweep voltammetry (LSV) normalized by Pd and Pt mass loading, the HEI_800/C needs an overpotential of only −0.128 V versus reference hydrogen electrode (RHE) to deliver 10 mA cm^{-2} (η_{10}, commonly used performance metrics for HER) which is much lower than HEI_400/C (−0.363 V), HEI_600/C (−0.248 V) and commercial Pt/C (−0.243 V) (Figure 5b,e). Lower overpotential means less energy waste, which is therefore desired for catalytic applications. The mass activity at the potential of −0.25 V versus RHE, shows the gradual increase from core-shell NP to HEI NPs from 3.7 A mg_{Pt+Pd}^{-1} to 26.82 A mg_{Pt+Pd}^{-1} (Figure S40). The mass activity of HEI_800/C NPs is 2.5 times higher than that of commercial Pt/C catalysts. The comparison of LSV curves normalized by geometric area also shows that the HEI_800 exhibits much better alkaline HER activity than both HEI_400/C and HEI_600/C, as well as the commercial Pt/C (Figure 5c). Tafel plots derived from LSV curves show that the HEI_800/C possesses the smallest Tafel slopes (21 mV dec^{-1} when mass normalized, 18 mV dec^{-1} when geometric area normalized),

suggesting its considerably enhanced alkaline HER kinetics (Figures 5d and S41). The geometric area-based current density depends on the electrode's electrochemically active surface area (ECSA). We note that for high-entropy systems, which contain a wide variety of metals and active sites, pinpointing specific active sites using a single electrochemical method like ECSA can be challenging.[51] To evaluate the intrinsic catalytic activity independently of ECSA, the current densities were normalized to the ECSA of each sample using two distinct methods: 1) by calculating the double-layer capacitance (Cdl) from a cyclic voltammogram recorded within a non-Faradaic potential window and 2) by performing CO stripping. The $ECSA_{Cdl}$ value of the HEI_600/C is higher than the HEI_400/C and HEI_800/C samples (Figure S42e). The ECSA normalized LSV plot shows higher activity per ECSA for HEI_800/C NPs (Figure S42f). The ECSAs of these catalysts were also measured by calculating the integrated charge from the CO oxidation peaks (Figure S43). The estimated $ECSA_{CO}$ values confirmed that HEI_600/C had the highest ECSA, followed by HEI_800/C and HEI_400/C. These findings suggest that HEI_600/C exposes more active sites than HEI_800/C, as expected, due to Pt migrating from the shell toward the center with increased mixing. However, the per-site activity of HEI_800/C is higher, resulting in overall greater current density and enhanced HER activity. These comparisons demonstrate that the crystal phase plays a vital role in governing the alkaline HER activity and the increased ordering degree due to diffusion can be tuned by surface ensemble engineering to enhance the alkaline HER activity.

Conclusion

A NP conversion strategy for synthesizing different monodisperse PE NPs has been demonstrated from core-shell precursor NPs. We systematically demonstrate the synthesis of PE NPs that include HEA, HEI, and multiphase NPs, by varying the stoichiometry and metal composition of precursor core-shell NPs. Results show that annealing nonequimolar core-shell NPs produces Janus-type NPs, while equimolar core-shell NPs lead to homogeneous mixing. Specifically, Ni promotes HEA formation, while Fe favors HEI formation, governed by ΔH_{mix} and ΔS_{mix}, as supported by atomistic simulations. We view this NP conversion strategy to PE NPs as highly modular, providing a programmable pathway to obtain size-tunable monodisperse samples with a wide range of compositions. Given the grounding of these synthetic outcomes in thermodynamic principles, we anticipate that computational screening can be leveraged in the future to predict the final thermodynamic phases of PE NPs when constructing precursor core-shell NPs with specific metal identities and ratios.

Author Contributions

N.K. and S.E.S. were responsible for the project concept and design of experiments. N.K. developed the synthesis of core-shell NPs, PE NPs, and characterizations. M.M. and R.S. helped in the synthesis of Au_2Cu and $AuCu_2$ NPs, respectively. A.L. contributed in theoretical simulations. This manuscript was written through the contributions of all authors. All authors have given approval to the final version of this manuscript.

Acknowledgements

S.E.S, N.K., M.M., and R.S. acknowledge financial support from Indiana University and the US National Science Foundation (NSF CHE 2203349). The authors acknowledge support from Indiana University's Electron Microscopy Center, XPS facility, and Nanoscale Characterization Facility for access to instrumentation. They also thank Dr. Shelby Radar, Dr. Maren Pink, and Dr. Yaroslav Losovyj for their helpful discussions. The simulation part of this research done by A.L. was supported in part by Lilly Endowment, Inc., through its support for the Indiana University Pervasive Technology Institute.

Conflict of Interests

The authors declare no conflict of interest.

Data Availability Statement

The data from this study are openly available in Zenodo at https://doi.org/10.5281/zenodo.15285357.

Keywords: High entropy alloy · High entropy intermetallic · High entropy nanoparticle · Polyelemental nanoparticle

[1] X. Chang, M. Zeng, K. Liu, L. Fu, *Adv. Mater.* **2020**, *32*, 1907226.
[2] M. V. Kovalenko, L. Manna, A. Cabot, Z. Hens, D. V. Talapin, C. R. Kagan, V. I. Klimov, A. L. Rogach, P. Reiss, D. J. Milliron, P. Guyot-Sionnnest, G. Konstantatos, W. J. Parak, T. Hyeon, B. A. Korgel, C. B. Murray, W. Heiss, *ACS Nano* **2015**, *9*, 1012–1057.
[3] W.-T. Koo, J. E. Millstone, P. S. Weiss, I.-D. Kim, *ACS Nano* **2020**, *14*, 6407–6413.
[4] Y. Li, Y. Liao, J. Zhang, E. Huang, L. Ji, Z. Zhang, R. Zhao, Z. Zhang, B. Yang, Y. Zhang, B. Xu, G. Qin, X. Zhang, *Angew. Chem. Int. Ed.* **2021**, *60*, 27113–27118.
[5] E. P. George, D. Raabe, R. O. Ritchie, *Nat. Rev. Mater.* **2019**, *4*, 515–534.
[6] Q. Ding, Y. Zhang, X. Chen, X. Fu, D. Chen, S. Chen, L. Gu, F. Wei, H. Bei, Y. Gao, M. Wen, J. Li, Z. Zhang, T. Zhu, R. O. Ritchie, Q. Yu, *Nature* **2019**, *574*, 223–227.
[7] J. Luo, X. Li, Y. Ye, T. Zhou, W. Wu, H. Li, Q. Yang, H. Yan, J. Zeng, *Angew. Chem. Int. Ed.* **2025**, *64*, e202419093.
[8] H. Cai, H. Yang, S. He, D. Wan, Y. Kong, D. Li, X. Jiang, X. Zhang, Q. Hu, C. He, *Angew. Chem. Int. Ed.* **2025**, *64*, e202423765.
[9] W.-L. Hsu, C.-W. Tsai, A.-C. Yeh, J.-W. Yeh, *Nat. Rev. Chem.* **2024**, *8*, 471–485.
[10] Y. Nakaya, S. Furukawa, *Chem. Sci.* **2024**, *15*, 12644–12666.
[11] H. Wang, P. Y. Yang, W. J. Zhao, S. H. Ma, J. H. Hou, Q. F. He, C. L. Wu, H. A. Chen, Q. Wang, Q. Cheng, B. S. Guo, J. C. Qiao,

W. J. Lu, S. J. Zhao, X. D. Xu, C. T. Liu, Y. Liu, C. W. Pao, Y. Yang, *Nat. Commun.* **2024**, *15*, 6782.
[12] T. Chen, C. Qiu, X. Zhang, H. Wang, J. Song, K. Zhang, T. Yang, Y. Zuo, Y. Yang, C. Gao, W. Xiao, Z. Jiang, Y. Wang, Y. Xiang, D. Xia, *J. Am. Chem. Soc.* **2024**, *146*, 1174–1184.
[13] S. Zheng, J. Hu, R. Feng, J. Xu, Y. Yu, L. Li, W. Liu, W. Zhang, F. Huo, F. Saleem, *Small Struct.* **2024**, *5*, 2300537.
[14] Y. Wang, N. Gong, H. Liu, W. Ma, K. Hippalgaonkar, Z. Liu, Y. Huang, *Adv. Mater.* **2023**, *35*, 2302067.
[15] D. Wang, Z. Chen, Y. Wu, Y.-C. Huang, L. Tao, J. Chen, C.-L. Dong, C. V. Singh, S. Wang, *SmartMat*, **2023**, *4*, e1117.
[16] T. Shen, D. Xiao, Z. Deng, S. Wang, L. An, M. Song, Q. Zhang, T. Zhao, M. Gong, D. Wang, *Angew. Chem.* **2024**, *136*, e202403260.
[17] P.-C. Chen, M. Liu, J. S. Du, B. Meckes, S. Wang, H. Lin, V. P. Dravid, C. Wolverton, C. A. Mirkin, *Science* **2019**, *363*, 959–964.
[18] C. Tan, H. Zhang, *Chem. Soc. Rev.* **2015**, *44*, 2713–2731.
[19] G. Chen, Y. Zhao, G. Fu, P. N. Duchesne, L. Gu, Y. Zheng, X. Weng, M. Chen, P. Zhang, C.-W. Pao, J.-F. Lee, N. Zheng, *Science* **2014**, *344*, 495–499.
[20] Y. Yao, Z. Huang, P. Xie, S. D. Lacey, R. J. Jacob, H. Xie, F. Chen, A. Nie, T. Pu, M. Rehwoldt, D. Yu, M. R. Zachariah, C. Wang, R. Shahbazian-Yassar, J. Li, L. Hu, *Science* **2018**, *359*, 1489–1494.
[21] M. Cui, C. Yang, S. Hwang, M. Yang, S. Overa, Q. Dong, Y. Yao, A. H. Brozena, D. A. Cullen, M. Chi, T. F. Blum, D. Morris, Z. Finfrock, X. Wang, P. Zhang, V. G. Goncharov, X. Guo, J. Luo, Y. Mo, F. Jiao, L. Hu, *Sci. Adv.* **2022**, *8*, eabm4322.
[22] D. Wu, K. Kusada, T. Yamamoto, T. Toriyama, S. Matsumura, S. Kawaguchi, Y. Kubota, H. Kitagawa, *J. Am. Chem. Soc.* **2020**, *142*, 13833–13838.
[23] G. Feng, F. Ning, J. Song, H. Shang, K. Zhang, Z. Ding, P. Gao, W. Chu, D. Xia, *J. Am. Chem. Soc.* **2021**, *143*, 17117–17127.
[24] G. R. Dey, S. S. Soliman, C. R. McCormick, C. H. Wood, R. R. Katzbaer, R. E. Schaak, *ACS Nanosci. Au* **2024**, *4*, 3–20.
[25] H. Luo, L. Li, F. Lin, Q. Zhang, K. Wang, D. Wang, L. Gu, M. Luo, F. Lv, S. Guo, *Adv. Mater.* **2024**, *36*, 2403674.
[26] M. Long, S. Lai, K. Miao, W. Jiang, W. Fan, X. Kang, *Angew. Chem.* **2025**, *137*, e202419956.
[27] Z. Zhang, P. Yu, Z. Liu, K. Liu, Z. Mu, Z. Wen, J. She, Y. Bai, Q. Zhang, T. Cheng, C. Gao, *J. Am. Chem. Soc.* **2025**, *147*, 9640–9652.
[28] G. R. Dey, C. R. McCormick, S. S. Soliman, A. J. Darling, R. E. Schaak, *ACS Nano* **2023**, *17*, 5943–5955.
[29] S. S. Soliman, G. R. Dey, C. R. McCormick, R. E. Schaak, *ACS Nano* **2023**, *17*, 16147–16159.
[30] J. K. Mathiesen, H. M. Ashberry, R. Pokratath, J. T. L. Gamler, B. Wang, A. Kirsch, E. T. S. Kjær, S. Banerjee, K. M. Ø. Jensen, S. E. Skrabalak, *ACS Nano* **2024**, *18*, 26937–26947.
[31] L. Yang, R. He, J. Chai, X. Qi, Q. Xue, X. Bi, J. Yu, Z. Sun, L. Xia, K. Wang, N. Kapuria, J. Li, A. Ostovari Moghaddam, A. Cabot, *Adv. Mater.* **2025**, *37*, 2412337.
[32] Y. Chen, X. Zhan, S. L. A. Bueno, I. H. Shafei, H. M. Ashberry, K. Chatterjee, L. Xu, Y. Tang, S. E. Skrabalak, *Nanoscale Horiz.* **2021**, *6*, 231–237.
[33] S. L. A. Bueno, A. Leonardi, N. Kar, K. Chatterjee, X. Zhan, C. Chen, Z. Wang, M. Engel, V. Fung, S. E. Skrabalak, *ACS Nano* **2022**, *16*, 18873–18885.
[34] N. Kar, M. McCoy, J. Wolfe, S. L. A. Bueno, I. H. Shafei, S. E. Skrabalak, *Nat. Synth.* **2023**, *3*, 175–184.
[35] D. Kim, J. Resasco, Y. Yu, A. M. Asiri, P. Yang, *Nat. Commun.* **2014**, *5*, 4948.
[36] S. Krouna, A. Acheche, G. Wang, N. O. Pena, R. Gatti, C. Ricolleau, H. Amara, J. Nelayah, D. Alloyeau, *Adv. Mater.* **2025**, *37*, 2414510.
[37] M. S. Daw, M. I. Baskes, *Phys. Rev. Lett.* **1983**, *50*, 1285–1288.
[38] J. T. L. Gamler, A. Leonardi, X. Sang, K. M. Koczkur, R. R. Unocic, M. Engel, S. E. Skrabalak, *Nanoscale Adv.* **2020**, *2*, 1105–1114.
[39] P. Scardi, A. Leonardi, L. Gelisio, M. R. Suchomel, B. T. Sneed, M. K. Sheehan, C.-K. Tsung, *Phys. Rev. B* **2015**, *91*, 155414.
[40] S. Zhang, S. Guo, H. Zhu, D. Su, S. Sun, *J. Am. Chem. Soc.* **2012**, *134*, 5060–5063.
[41] Y. Wang, M. Jiang, R. Wang, Z. Wen, H. Li, Y. Ren, G. Qin, *Acta Mater.* **2022**, *235*, 118058.
[42] H. M. Ashberry, J. T. L. Gamler, R. R. Unocic, S. E. Skrabalak, *Nano Lett.* **2019**, *19*, 6418–6423.
[43] W.-J. Zeng, C. Wang, Q.-Q. Yan, P. Yin, L. Tong, H.-W. Liang, *Nat. Commun.* **2022**, *13*, 7654.
[44] C.-H. Cui, S.-H. Yu, *Acc. Chem. Res.* **2013**, *46*, 1427–1437.
[45] Q. Wang, Y. Qin, J. Xie, Y. Kong, Q. Sun, Z. Wei, S. Zhao, *Adv. Mater.* **2025**, *37*, 2420173.
[46] C. Wei, R. R. Rao, J. Peng, B. Huang, I. E. L. Stephens, M. Risch, Z. J. Xu, Y. Shao-Horn, *Adv. Mater.* **2019**, *31*, 1806296.
[47] A. Lasia, *Int. J. Hydrog. Energy* **2019**, *44*, 19484–19518.
[48] N. Mahmood, Y. Yao, J.-W. Zhang, L. Pan, X. Zhang, J.-J. Zou, *Adv. Sci.* **2018**, *5*, 1700464.
[49] M. Sankar, N. Dimitratos, P. J. Miedziak, P. P. Wells, C. J. Kiely, G. J. Hutchings, *Chem. Soc. Rev.* **2012**, *41*, 8099.
[50] J. Greeley, I. E. L. Stephens, A. S. Bondarenko, T. P. Johansson, H. A. Hansen, T. F. Jaramillo, J. Rossmeisl, I. Chorkendorff, J. K. Nørskov, *Nat. Chem.* **2009**, *1*, 552–556.
[51] M. Shao, J. H. Odell, S.-I. Choi, Y. Xia, *Electrochem. Commun.* **2013**, *31*, 46–48.

Manuscript received: March 09, 2025
Revised manuscript received: April 07, 2025
Accepted manuscript online: April 20, 2025
Version of record online: May 02, 2025